Published in final edited form as:
Phys Med Biol. 2010 March 7; 55(5): 1453–1473. doi:10.1088/0031-9155/55/5/013.

Noise and signal properties in PSF-based fully 3D PET image reconstruction: an experimental evaluation

S Tong, **A M Alessio**, and **P E Kinahan**
Department of Radiology, University of Washington, Seattle, WA 98195, USA

S Tong: saratong@u.washington.edu

Abstract

The addition of accurate system modeling in PET image reconstruction results in images with distinct noise texture and characteristics. In particular, the incorporation of point spread functions (PSF) into the system model has been shown to visually reduce image noise, but the noise properties have not been thoroughly studied. This work offers a systematic evaluation of noise and signal properties in different combinations of reconstruction methods and parameters. We evaluate two fully 3D PET reconstruction algorithms: (1) OSEM with exact scanner line of response modeled (OSEM+LOR), (2) OSEM with line of response and a measured point spread function incorporated (OSEM+LOR +PSF), in combination with the effects of four post-reconstruction filtering parameters and 1–10 iterations, representing a range of clinically acceptable settings. We used a modified NEMA image quality (IQ) phantom, which was filled with ^{68}Ge and consisted of six hot spheres of different sizes with a target/background ratio of 4:1. The phantom was scanned 50 times in 3D mode on a clinical system to provide independent noise realizations. Data were reconstructed with OSEM+LOR and OSEM+LOR+PSF using different reconstruction parameters, and our implementations of the algorithms match the vendor's product algorithms. With access to multiple realizations, background noise characteristics were quantified with four metrics. Image roughness and the standard deviation image measured the pixel-to-pixel variation; background variability and ensemble noise quantified the region-to-region variation. Image roughness is the image noise perceived when viewing an individual image. At matched iterations, the addition of PSF leads to images with less noise defined as image roughness (reduced by 35% for unfiltered data) and as the standard deviation image, while it has no effect on background variability or ensemble noise. In terms of signal to noise performance, PSF-based reconstruction has a 7% improvement in contrast recovery at matched ensemble noise levels and 20% improvement of quantitation SNR in unfiltered data. In addition, the relations between different metrics are studied. A linear correlation is observed between background variability and ensemble noise for all different combinations of reconstruction methods and parameters, suggesting that background variability is a reasonable surrogate for ensemble noise when multiple realizations of scans are not available.

1. Introduction

Iterative reconstruction methods are widely used in positron emission tomography (PET) clinical practice because they offer an improved contrast to noise performance over analytic algorithms (Riddel *et al* 2001, Son *et al* 2003). Several advances to iterative reconstruction methods have enabled this improved performance. For example, the attenuation-weighted ordered subsets expectation-maximization (AW-OSEM) (Comtat *et al* 1998), moves the attenuation correction into the reconstruction matrix, and helps to preserve Poisson statistics. Performance of iterative reconstruction could be further improved when the full physics of the imaging process is accurately and precisely modeled. Several works reconstruct directly from the raw coincidence line-of-response (LOR) data without any pre-processing (Kadrmas 2004, 2008), and are called the LOR-based algorithms. The Poisson statistics of the

measurements are preserved in these algorithms, and the full benefit of maximum-likelihood (ML) reconstruction is achieved. One important component of the physics modeling is the detector point spread function (PSF), which could be obtained through analytical derivations (Strul *et al* 2003), Monte Carlo simulations (Qi *et al* 1998, Alessio *et al* 2006) or experimental measurements (Panin *et al* 2006). Modeling of the detector PSF during fully 3D iterative reconstruction has been shown to improve the spatial resolution, and to generate visually less noisy images. However, the noise properties of the PSF-based reconstruction algorithms have not been thoroughly evaluated.

Noise characteristics in reconstruction have important implications for quantitation and detection performance in PET imaging, and accordingly there have been abundant efforts devoted to the analysis of noise properties in PET image reconstruction, which could largely be classified into two categories. The first category of works use theoretical derivation to obtain analytical expressions for the ensemble noise properties. Since most iterative algorithms for PET reconstruction are nonlinear, the statistical properties of the reconstructed images cannot be computed directly from those of the data, and approximations are usually required to make the problem tractable. By linearizing the ML-EM algorithm in log-image space and making certain approximations, Barrett *et al* (1994) derived a theoretical formulation by which the ensemble statistical properties of the EM algorithm could be obtained at each iteration. This work was validated through Monte Carlo methods in their later work (Wilson *et al* 1994), in which the algorithm was linearized in the image space. Many other works have examined the ensemble noise properties for regularized EM reconstruction (Fessler 1996, Wang and Gindi 1997), and in particular Qi and Leahy studied the noise properties of maximum *a posteriori* (MAP) reconstruction for fully 3D PET (Qi and Leahy 2000). The noise characterization of block-iterative reconstruction algorithms is presented in the work of Soares *et al* (2000), which made the assumption that the noise in the reconstructed images is small compared to the mean image. While these works provide solid theoretical basis for quantifying the noise in reconstruction, the computation cost is typically high and the accuracy of the approximation may deteriorate at higher iterations (Qi and Leahy 2000). In particular, due to the high variance behavior at high iteration numbers, EM- and OSEM-type algorithms are typically regularized through early termination of the algorithms or by subsequent smoothing of the reconstructed images. Hence, it is also necessary to study how noise characteristics change with different settings of reconstruction parameters (number of iterations, post-smoothing, etc) through experimental methods.

The other category of noise analysis works perform experimental evaluation of noise properties through Monte Carlo simulations or on measured data sets. Different image figures of merit (FOMs) have been adopted to evaluate the influence of reconstruction parameters. As a validation for their earlier work (Soares *et al* 2000), Soares *et al* studied noise characterization of 2D block-iterative reconstruction algorithms (including OSEM) through Monte Carlo simulations (Soares *et al* 2005). Resolution recovery of 2D AW-OSEM reconstruction was presented in Bernardi *et al* (2007), where algorithm properties in terms of contrast recovery, image noise and object separability were evaluated on scanned sphere phantom studies. More recently, Kadrmas *et al* evaluated the lesion detection performance of four popular 3D PET reconstruction algorithms on a multi-compartment anthropomorphic phantom (Kadrmas *et al* 2009). Different lesion sizes and target-to-background ratios were studied, and the detectability was assessed by localization receiver operating characteristics methods. For the clinical task of quantification, several works have evaluated the effects of different reconstruction parameters on image noise and accuracy of standard uptake values (SUVs). Based on simulations on a thorax phantom, Boellaard *et al* assessed how the accuracy of SUVs is affected by different tumor sizes, target-to-background ratios, sinogram noise levels, post-filtering and region of interest (ROI) definitions in 2D OSEM reconstructions (Boellaard *et al* 2004). A similar study on patient tumor data was performed in the work of Jaskowiak *et*

al (2005), where the influence of reconstruction iterations on SUVs is studied for 2D OSEM reconstruction. Boellaard *et al* found large variation in SUV estimations (≥50%) depending on all parameters studied (Boellaard *et al* 2004), and Jaskowiak *et al* showed that SUV measures are statistically different across different iteration groups (Jaskowiak *et al* 2005). These studies have shown that image noise properties vary substantially for different combinations of reconstruction parameters in 2D OSEM algorithms.

With the advances in 3D PET reconstruction algorithms, some studies have shown that the addition of accurate system modeling leads to images with improved quantitative accuracy and contrast to noise performance. However, the noise characteristics in PSF-based reconstruction have not been thoroughly studied in the literature. In this work, we present a systematic evaluation of noise and signal properties in different combinations of reconstruction methods and parameters for 3D PET image reconstruction. We evaluate two algorithms: OSEM+LOR (OSEM with exact locations of the line of response modeled) and OSEM+LOR+PSF (OSEM +LOR with point spread function modeled), in combination with the effects of four post-reconstruction filtering parameters and up to ten iterations. Our evaluation is across clinically acceptable range of iterations. The OSEM+LOR implementation matches the vendor's product reconstruction and data correction (randoms, scatter, deadtime, efficiency, etc) methods, providing insight into actual system performance. The evaluation is based on 50 independent realizations of measured phantom data. We adopt four metrics to quantify the background noise properties, and five metrics to evaluate the signal and noise characteristics in features. We use theoretical derivation to study how the noise metrics relate to image variance and covariance. We assess the performance of the two reconstruction algorithms, as well as how different reconstruction parameters affect the noise properties. The relations between various metrics are also studied over a range of reconstruction parameters.

2. Methods

2.1. Phantom experiments

We used a modified NEMA NU-2 image quality (IQ) phantom in the study. The modified phantom consists of an anthropomorphic chamber which contains six hot spheres with inner diameters of 10, 13, 17, 22, 28 and 37 mm (Doot *et al* 2007). The central 5 cm diameter 'lung' cylinder in the original NEMA phantom was removed, and the two larger hollow spheres were changed to hot spheres, as opposed to the cold spheres in NEMA NU-2 instructions (NEMA 2001). Phantom spheres and background volumes were filled with long half-life ^{68}Ge solid epoxy ($T_{1/2}$ = 270.8 days), with a fixed target/background ratio of 4:1. On the day of the experiments, the total activity in the phantom was 47.22 MBq, and the background activity concentration level was 4.55 kBq mL^{-1}.

The phantom described above was scanned on a discovery-STE (DSTE) PET/CT scanner (GE Healthcare). The phantom was positioned off the center of the transaxial field of view (FOV), and the acquisitions were obtained in fully 3D mode. Fifty 5 min acquisitions of the phantom were obtained, generating 50 independent realizations of data. Each data set contained roughly 85 million prompts. The CT scan consisted of 84 slices, and was later used for attenuation correction.

2.2. Image reconstruction

All 50 scans were reconstructed with each of the two methods mentioned earlier. By using the scanner manufacturer's software, our implementations of the reconstruction algorithms are similar to the scanner reconstruction. The specific implementation of the OSEM+LOR algorithm is derived from the work of Manjeshwar *et al* (2006) and reconstructs using angular subsets and all oblique planes from the fully 3D data (no axial mashing). Based on a distance-

driven projector design, the algorithm allows accurate modeling of the native block-based detector geometry. The algorithm also incorporates the corrections for crystal efficiency, detector deadtime, attenuation, random and scatter coincidences inside the iterative loop in order to preserve Poisson statistics of the measurements. For the OSEM+LOR+PSF algorithm, the scanner point spread function (PSF) is included in the OSEM+LOR reconstruction (Alessio *et al* 2009). Previous studies have shown that in-plane parallax error is the most spatially variant resolution component, and most of the system resolution losses could be recovered with a simple radially blurring system model (Alessio *et al* 2006). The PSF used in the current work models the detector blurring as a 2D system response function, which blurs in the radial direction and is variant with radial position. The PSF is obtained through experimental measurement with a non-collimated point source (Alessio *et al* 2005), and the effects of inter-crystal scatter, penetration, photon pair non-collinearity and positron range are taken into account. The blurring terms were incorporated in a factorized system model and applied during each call to the system matrix, both in the forward and backward projection steps.

Each of the 50 independent acquisitions was reconstructed onto 47 slices of 256 × 256 image matrices, corresponding to a voxel size of 2.73 × 2.73 × 3.27 mm^3. Each reconstruction was run to 10 iterations with 28 subsets for each iteration, and the results of each iteration were saved. The addition of the PSF model to OSEM+LOR increased the reconstruction time by 3.2%.

After the reconstruction step, different post-smoothing filters were applied to the reconstructed images. The images either had no post-reconstruction smoothing applied, or were convolved with 4 mm, 7 mm or 10 mm 2D Gaussian filters, where the filtering parameters were chosen to include typical settings used clinically. To match the vendor's product implementation, the same smoothing in the axial direction was also included for each Gaussian filter by performing a weighted average of adjacent image slices.

Finally, the reconstruction and processing steps produced a series of reconstructed images with different combinations of reconstruction methods and parameters: 2 reconstruction methods × 4 levels of post-reconstruction filters × 10 iterations × 50 realizations, for a total of 4000 image volumes. Different image figures of merit (FOMs) were adopted to evaluate the noise characteristics for the two reconstruction methods and various reconstruction parameters.

2.3. Noise properties in background

With access to multiple acquisitions of the phantom, we use four image FOMs: image roughness, background variability, ensemble noise and the standard deviation image, to quantify the background noise characteristics. The relations between these FOMs are also studied.

To calculate the noise metrics, one image slice containing all the six hot spheres (shown in figure 1(a)) was selected as the target slice for analysis. 2D ROIs over slices suggested in NEMA NU-2 instructions (NEMA 2001) were used in our work. We positioned 12 background 2D ROIs on the target slice, as well as on 4 neighboring slices (slices ±13 mm and ±26 mm away), for a total of 60 background ROIs for each ROI size. Six different ROI sizes were used, and the ROI diameters were equal to the physical inner diameters of the hot spheres. Figure 1 (b) shows the 37 mm diameter ROIs overlaid on the target slice.

The reconstructed background activity is modeled as

$$f_{ir}=b_0+n_{ir} \quad (1)$$

where f_{ir} is the reconstructed value at pixel i for realization r, b_0 is the true background activity and n_{ir} is the corresponding noise term.

For realization r, the mean of pixels in the kth ROI ($k = 1, 2, \ldots, K$ and $K = 60$ for background ROIs) is denoted as

$$m_{r,k}=\frac{1}{I}\sum_{i\in \mathrm{ROI}_k} f_{ir} \tag{2}$$

where I is the number of pixels in ROI_k.

The noise metrics are defined and calculated as follows.

2.3.1. Image roughness (IR)—Image roughness measures the pixel to pixel variability in the image, and could be calculated for a single realization. Image roughness is the image noise perceived when viewing an individual image. For ROI_k and realization r, image roughness is defined as the coefficient of variation (COV) of the pixel values as

$$\mathrm{IR}_{r,k}=\frac{\sqrt{\frac{1}{I-1}\sum_{i\in \mathrm{ROI}_k}(f_{ir}-m_{r,k})^2}}{m_{r,k}}. \tag{3}$$

Note that this value is defined for each realization and ROI, so we average the value over the 60 ROIs to generate the final image roughness $\mathrm{IR}_r=\frac{1}{K}\sum_{k=1}^{K}\mathrm{IR}_{r,k}$. Since IR_r is defined for each realization, we could further calculate its mean and standard deviation across different realizations.

2.3.2. Background variability (BV)—This is a measure for background variability proposed in the NEMA NU-2 instructions (NEMA 2001). This metric is also calculated for a single realization, and is defined as the COV of the ROI means $m_{r,k}$ across the 60 ROIs as

$$\mathrm{BV}_r=\frac{\sqrt{\frac{1}{K-1}\sum_{k=1}^{K}(m_{r,k}-\overline{m}_r)^2}}{\overline{m}_r} \tag{4}$$

where $\overline{m}_r=\frac{1}{K}\sum_{k=1}^{K}m_{r,k}$ is the average of ROI means over different ROIs, and K is the number of ROIs ($K = 60$ for background ROIs). As this metric is defined for each realization r, we could compute its variation across realizations when multiple realizations are available.

2.3.3. Ensemble noise (EN)—Ensemble noise is a measure for noise across independent realizations, and it is inversely proportional to detection task performance. For each ROI_k, it is defined as the COV of ROI means $m_{r,k}$ across the 50 realizations:

$$\mathrm{EN}_k=\frac{\sqrt{\frac{1}{R-1}\sum_{r=1}^{R}(m_{r,k}-\overline{m}_k)^2}}{\overline{m}_k} \tag{5}$$

where $\overline{m}_k=\frac{1}{R}\sum_{r=1}^{R} m_{r,k}$ is the average of ROI means over realizations, and R is the number of realizations (R = 50 for our analysis). EN_k is defined for each ROI_k, and we further average this value over ROIs to generate the final ensemble noise $EN=\frac{1}{K}\sum_{k=1}^{K} EN_k$. This metric can only be computed when multiple realizations are available.

2.3.4. Standard deviation image—For each pixel in the target slice, we calculate the sample standard deviation across different realizations, and generate the standard deviation image. Pixel i in the standard deviation image is defined as

$$\widehat{\sigma}_i=\sqrt{\frac{1}{R-1}\sum_{r=1}^{R}(f_{ir}-\overline{f}_i)^2} \tag{6}$$

where $\overline{f}_i=\frac{1}{R}\sum_{r=1}^{R} f_{ir}$ is the pixel average over realizations. $\hat{\sigma}_i$ is an estimate of the ensemble standard deviation. The standard deviation image is defined for each pixel of the slice (not restricted to background pixels), and it offers an effective way to compare noise standard deviation (or variance) in different reconstruction methods and parameters.

In our study, the first three noise metrics (IR, BV, and EN) are all defined as coefficient of variation, which can be considered as a normalized measure of dispersion, i.e. the ratio of the standard deviation to the mean value. They could also be defined directly as the sample standard deviation without the normalization term. We use the definitions with the coefficient of variation in order to compare the metrics more easily.

Among the four metrics defined above, ensemble noise and the standard deviation image are based on reconstruction results from different realizations, and are often considered to be closely related to the 'true' noise which most accurately represents the uncertainties in the images. However, as multiple realizations of acquisitions are usually not available in many cases, metrics defined on a single realization, such as image roughness and background variability, are more often used to quantify the noise characteristics. While these two metrics have been used extensively in the literature to assess the performance of different reconstruction algorithms or different imaging system configurations, their relation has not been properly studied, and in particular, how these metrics relate to the ensemble noise is not clear. Therefore, we also analyze the relations between different metrics.

The possible dimensions of variations for the metrics include 2 reconstruction methods × 4 levels of post-reconstruction filters × 6 ROI sizes × 10 iterations × 50 realizations.

2.4. Signal and noise properties in features

The reconstructed signal in the hot spheres is modeled as

$$f_{ir}=f_0+n_{ir} \tag{7}$$

where f_{ir} is the reconstructed value at pixel i for realization r, f_0 is the true activity in hot spheres and n_{ir} is the corresponding noise term.

We evaluated several signal strength metrics to assess signal versus noise performance with different reconstruction methods and parameters. We placed six 2D ROIs covering the six hot spheres, and the ROI diameters match the physical inner diameters of the spheres. The ROI index $k = 1, 2, \ldots, 6$ denotes each of the six hot spheres. Note that this is slightly different from the study of background noise, where 60 ROIs were used for each of the 6 ROI sizes. The following metrics are used in the analysis of signal and noise properties in hot spheres.

2.4.1. Contrast recovery coefficient of mean value (CRCmean)—For one realization, CRCmean is defined for each sphere as

$$\mathrm{CRCmean}_{r,k} = \frac{m_{r,k}}{f_0} \tag{8}$$

where $m_{r,k}$ is the region average for each hot sphere as defined in equation (2).

2.4.2. Contrast recovery coefficient of maximum value (CRCmax)—CRCmax is defined for each realization r and hot sphere k as

$$\mathrm{CRCmax}_{r,k} = \frac{\max_{r,k}}{f_0} \tag{9}$$

where $\max_{r,k}$ is the maximum pixel value in sphere k.

2.4.3. Ensemble noise in hot spheres (EN_{HS})—Ensemble noise is defined the same way as in equation (5). EN_k is directly used in the analysis as ensemble noise for each of the six hot spheres, and no further average over ROIs is performed as in background analysis.

2.4.4. Signal to noise ratio for quantitation (SNRquant)—SNRquant, a measure of ROI accuracy and precision, has been proposed as a practical metric for representing quantitation performance (Barrett 1990). It is defined for each hot sphere k as

$$\mathrm{SNRquant}_k = \frac{f_0}{\sqrt{\frac{1}{R}\sum_{r=1}^{R}(m_{r,k} - f_0)^2}}. \tag{10}$$

2.4.5. SNR non-prewhitening filter (SNRnpw)—SNRnpw has been used as a measurement of detection task performance in binary classification problems (Barrett 1990, Sharp *et al* 1996) and is defined here as

$$\mathrm{SNRnpw}_k = \frac{\overline{m}_k^{\mathrm{feature}} - \overline{m}_k^{\mathrm{background}}}{\sqrt{(s_1^2 + s_0^2)/2}} \tag{11}$$

where $\overline{m}_k^{\mathrm{feature}} = \frac{1}{R}\sum_{r=1}^{R} m_{r,k}$ is the average of sphere means over realizations on a target present ($t = 1$) slice, $\overline{m}_k^{\mathrm{background}}$ is the same average on a target absent ($t = 0$) slice and s_1 and s_0 are the

corresponding sample standard deviations through all realizations, i.e. $s_1 = \sqrt{\frac{1}{R-1}\sum_{r=1}^{R}(m_{r,k} - \overline{m}_k)^2}$ on the target present slice, and s_0 is calculated the same way on the target absent slice. We use the same slice for background analysis (a slice containing all six hot spheres) as the target present slice, and a slice 39 mm away as the target absent slice.

Among the five metrics defined above, $\mathrm{CRCmean}_{r,k}$ and $\mathrm{CRCmax}_{r,k}$ can be computed for each realization r, so we can further calculate their means and standard deviations across different realizations. The calculation of the other three metrics requires information from multiple realizations.

The total possible dimensions of variations for the five metrics include 2 reconstruction methods × 4 levels of post-reconstruction filters × 6 sphere sizes × 10 iterations × 50 realizations.

3. Relations of noise metrics to image variance and covariance

3.1. Theoretical derivation

To understand the properties of the noise metrics, we derive how our background noise metrics relate to the true noise variance and covariance. For simplicity of the derivation, we assume that the noise term n_{ir} in equation (1) has the same variance σ_b^2 for background pixels, so all pixel values f_{ir} in the background are identically distributed with variance σ_b^2. Note that we do not assume that the noise n_{ir} is zero-mean, since there could be bias in the reconstructed signal. We also make no assumption on statistical independence for distinct pixels in equation (1), so f_{ir} can be spatially correlated in our model (though not explicitly modeled).

For notational simplicity, we drop the ROI index k in the following derivation. We also define the noise metrics in a simplified version: the metrics are defined directly as the sample standard deviation without the normalization term. Note that this simplified version of definition differs from the ones used in section 2.3 only by a scaling factor. We adopt the new definition only for notational simplicity; the analysis below is also valid for the original definitions in section 2.3.

Recall that the ROI mean value is defined as $m_r = \frac{1}{I}\sum_{i\in\mathrm{ROI}} f_{ir}$ (I is the number of pixels in the ROI). Due to the spatial correlation of f_{ir}, m_r is the average of several correlated random variables, so the variance of the ROI mean m_r is formed from the sum of the variances and covariances of each pixel as

$$\mathrm{Var}(m_r) = \frac{1}{I^2}\left(I\sigma_b^2 + \sum_{i\neq j}\mathrm{Cov}(f_{ir}, f_{jr})\right) \tag{12}$$

where Var and Cov denote variance and covariance, respectively, and the summation of covariances is over i and j.

The simplified version of image roughness is defined as $\mathrm{IR}_r = \sqrt{\frac{1}{I-1}\sum_{i\in\mathrm{ROI}}(f_{ir} - m_r)^2}$. The square of IR_r could be further arranged as

$$\begin{aligned}\mathrm{IR}_r^2 &= \frac{1}{I-1}\sum_{i\in \mathrm{ROI}}(f_{ir}^2 - 2f_{ir}m_r + m_r^2)\\ &= \frac{1}{I-1}\left(\sum_{i\in \mathrm{ROI}} f_{ir}^2 - 2m_r I m_r + \sum_{i\in \mathrm{ROI}} m_r^2\right)\\ &= \frac{1}{I-1}\left(\sum_{i\in \mathrm{ROI}} f_{ir}^2 - I m_r^2\right).\end{aligned} \tag{13}$$

Due to the noise correlation, IR_r^2 (i.e. sample variance) is no longer an unbiased estimate of the true variance σ_b^2, and from equation (13) the expectation of IR_r^2 could be calculated as

$$\begin{aligned}E[\mathrm{IR}_r^2] &= \frac{1}{I-1}\left(\sum_{i\in \mathrm{ROI}} E[f_{ir}^2] - IE[m_r^2]\right)\\ &= \frac{1}{I-1}\left[\sum_{i\in \mathrm{ROI}}(\mathrm{Var}(f_{ir}) + E[f_{ir}]^2) - I(\mathrm{Var}(m_r) + E[m_r]^2)\right]\end{aligned} \tag{14}$$

where $E[]$ denotes mathematical expectation. By substituting equation (12) into the above equation and letting $E[f_{ir}] = m_0$, we have

$$\begin{aligned}E[\mathrm{IR}_r^2] &= \frac{I}{I-1}\left(\sigma_b^2 + m_0^2 - \frac{1}{I^2}\left(I\sigma_b^2 + \sum_{i\neq j}\mathrm{Cov}(f_{ir}, f_{jr})\right) - m_0^2\right]\\ &= \sigma_b^2 - \frac{1}{(I-1)I}\sum_{i\neq j}\mathrm{Cov}(f_{ir}, f_{jr}).\end{aligned} \tag{15}$$

The standard deviation image is based on independent samples of f_{ir} over realizations, so $\widehat{\sigma}_i^2$ would be an unbiased estimate of σ_b^2 for background pixels, i.e.

$$E[\widehat{\sigma}_i^2] = \sigma_b^2. \tag{16}$$

The simplified version of ensemble noise is defined as the sample standard deviation of ROI mean value m_r over realizations $\mathrm{EN} = \sqrt{\frac{1}{R-1}\sum_{r=1}^{R}(m_r - \overline{m})^2}$. Since different realizations have independent noise, sample variance of m_r (i.e. square of EN) is an unbiased estimate of the true variance of m_r, so

$$E[\mathrm{EN}^2] = \mathrm{Var}(m_r) = \frac{\sigma_b^2}{I} + \frac{1}{I^2}\sum_{i\neq j}\mathrm{Cov}(f_{ir}, f_{jr}). \tag{17}$$

Equations (15)–(17) describe how the background noise metrics relate to the ensemble noise variance and covariance. These equations will be used later to analyze the performance of various metrics for different reconstruction methods and parameters. In equation (15), the first term σ_b^2 has more contribution than the covariance term, so we would expect that image roughness is relatively insensitive to the ROI size. In equation (17), the noise variance σ_b^2 is

normalized by the number of pixels in the ROI, so we would expect that ensemble noise will decrease with ROI size. Noise covariance also affects image roughness and ensemble noise differently. Positive noise correlation will lead to smaller image roughness but larger ensemble noise.

In the above derivations, we assume that all background pixels f_{ir} have the same ensemble mean and variance. This is a reasonable assumption, since only one ROI is involved in the definitions of image roughness and ensemble noise. In reality, non-uniformity may exist in the reconstructed images (e.g. due to inaccurate corrections), so pixels in different regions can have different mean values. Background variability measures the variation of ROI means over multiple ROIs (definition in equation (4)), so this measure would be sensitive to background non-uniformity.

3.2. Estimation of noise variance and Covariance

As shown in equations (15) and (17), both image roughness and ensemble noise are affected by a noise variance term and a covariance term. In an effort to quantify the relative contributions of variance and covariance to noise metrics, we estimate noise variance and average covariance based on the above derivation.

We define $\bar{C}$ as the average of covariance terms in an ROI as

$$\bar{C}=\frac{\sum_{i\neq j}\mathrm{Cov}(f_{ir},f_{jr})}{(I-1)I}. \tag{18}$$

With this definition, we can solve σ_b^2 and $\bar{C}$ from equations (15) and (17) as

$$\sigma_b^2=\frac{I-1}{I}E[\mathrm{IR}_r^2]+E[\mathrm{EN}^2] \tag{19}$$

$$\bar{C}=E[\mathrm{EN}^2]-\frac{1}{I}E[\mathrm{IR}_r^2]. \tag{20}$$

We can obtain estimates of σ_b^2 and $\bar{C}$ using the results of noise metrics. We placed one single ROI in the background, and calculated image roughness and ensemble noise. Eight ROI sizes were used, with diameters equal to 10, 13, 17, 22, 28, 37, 44 and 49 mm. Then the average of IR_r^2 over 50 realizations is used as an estimate of $E[\mathrm{IR}_r^2]$, and EN^2 is used as an estimate of $E[\mathrm{EN}^2]$. Noise variance and average ROI covariance are estimated using equations (19) and (20). The estimated σ_b^2 and $\bar{C}$ results are presented in section 4.1.

4. Results

Figures 2 and 3 show example reconstructed images from one of the 50 realizations at iteration 2 and 8. From visual inspection, we observe differences in noise texture for different reconstruction methods. Specifically, PSF-based reconstruction results appear to be less noisy and to have a noise texture with larger correlations. We also observe variations of noise characteristics over different post-filters and iterations. Objective evaluation of these noise properties is presented in the following.

4.1. Background analysis results

Figure 4 presents the results for the first three background noise metrics which are defined in section 2.3, namely image roughness, background variability and ensemble noise. Each row of the figure corresponds to one noise metric. For plots on the left column, the ROI size is fixed (ROI = 22 mm corresponds to the ROI with 22 mm diameter), and the metric is plotted as a function of the iteration number. For plots on the right column, iteration number is fixed, and the metric is plotted as a function of the ROI size. Each of the six plots in figure 4 includes variations of two reconstruction algorithms (represented by black and red curves) and four post-filtering options (represented by different line styles). Since image roughness and background variability are defined on one realization, the mean of the metrics over 50 realizations is plotted in figure 4 (top and middle rows), with the error bars denoting standard deviation across realizations. In this way, the two plots on each row of figure 4 capture all the variations of the corresponding noise metric in that row.

From figure 4, it is observed that all the three background noise metrics decrease with post-filters applied, and increase with iteration number. Image roughness has a small increase for larger ROIs, while background variability and ensemble noises go down quickly with increasing ROI size. Comparing the two reconstruction methods at matched iterations, the incorporation of PSF, with other parameters fixed, reduces image roughness by ~35% for the unfiltered data. With increasing post-filtering, this difference between the two methods gets smaller. At matched iterations, the addition of the PSF offers no significant difference in background variability or ensemble noise.

All three noise metrics are defined as coefficients of variation, and their relations are studied by plotting one metric against another. In figure 5, image roughness (IR) and background variability (BV) are plotted against ensemble noise (EN). In plots on the left column, we fix the ROI size and study how the relation changes with different reconstruction methods and post-filtering options, while in plots on the right column, we evaluate how the metric relation changes for various reconstruction methods and ROI sizes, with no post-filtering applied. The top row of figure 5 plots the average image roughness over realizations versus the ensemble noise. It shows that while the mean of image roughness (over 50 realizations) increases monotonically with ensemble noise, there is not a linear relationship between the two metrics. The bottom row is related to the background variability. From these plots, a linear correlation is observed for the mean of background variability (across 50 realizations) and the ensemble noise. This linear relation follows a line near the identity line, and has a similar trend for different reconstruction methods, post-filters and ROI sizes. The error bars in the plots denote standard deviations across realizations, showing that background variability from one realization (represented by a line within the error bars) would also linearly correlate with the ensemble noise.

Results of the standard deviation image are presented in figure 6. Comparing the images on top and bottom rows (corresponding to OSEM+LOR and OSEM+LOR+PSF), we observe reduced sample standard deviation for PSF-based reconstruction. For a quantitative comparison, we placed 12 background 2D ROIs (as defined in section 2.3, of 22 mm diameter) on the standard deviation image, and calculated the ROI average. In figure 6, the ROI mean values are shown above each corresponding image, and these values confirm that PSF-based reconstruction has smaller sample standard deviation at matched iterations. As discussed earlier, each pixel in the standard deviation image $\hat{\sigma}_i$ is an estimate of the ensemble noise standard deviation, so reduced $\hat{\sigma}_i$ values indicate that PSF-based reconstructions have less noise at matched iterations. This effect is observed in both the background and hot spheres, and the difference between the two methods gets smaller with increasing post-filtering.

For each background pixel in the standard deviation image, the value $\hat{\sigma}_i$ could be normalized with the pixel average over realizations, $\bar{f}_i$, to generate a new metric $\hat{\sigma}_i/\bar{f}_i$ (see equation (6) for details). Comparing with the definition of ensemble noise in equation (5), we see that $\hat{\sigma}_i/\bar{f}_i$ is equivalent to the ensemble noise in the ROI of one pixel, so we call the new metric $EN_{onepixel}$. $EN_{onepixel}$ is a measure of the noise in a single pixel, and is similar to image roughness (IR) in this aspect. We plot the ratio of the metrics $IR/EN_{onepixel}$ as a function of ROI size in figure 7. From the definitions in equations (4) and (5), both background variability and ensemble noises are measures of variation in the ROI mean value. We also plot how the ratio of these two metrics BV/EN changes with ROI size in figure 7.

Results on the estimated noise variance σ_b^2 and the average ROI noise covariance $\bar{C}$ are presented in figure 8. The estimated noise variance increases with iteration number, and decreases with post-filters applied. The incorporation of PSF leads to reduced noise variance at matched iterations, and this effect gets smaller with the increasing post-filter level. These observations are consistent with the standard deviation image results. The addition of PSF leads to increased average ROI noise covariance, and hence increased noise correlation (considering smaller noise variance). For larger ROI size, the average noise covariance gets smaller. This is consistent with the definition of $\bar{C}$ in equation (18), since many close-to-zero covariance terms are included in the average for larger ROIs. Across all iterations and post-filtering levels, the estimated noise variance is at least one order magnitude larger than the average ROI noise covariance, suggesting that the variance term has more contribution for image roughness and ensemble noise in equations (15) and (17).

4.2. Feature analysis results

Figure 9 presents the results for contrast recovery coefficients. As was done for the background noise measures in figure 4, two plots are used to describe one metric in one row. Plots in the left column plot the metrics versus iteration number with the sphere fixed, while in the right column the metrics are plotted against sphere size with a fixed iteration number. We observe that both CRCmean and CRCmax increase with iteration and decrease with post-filtering, and more accurate CRCmean and CRCmax (i.e. values closer to 1) are obtained for larger sphere sizes. Comparing the two reconstruction methods, the incorporation of PSF improves the accuracy of CRCmean by ~7%, and this improvement is similar for all post-filtering options. A similar improvement (~16%) exists for the accuracy of CRCmax in unfiltered results, and this improvement is reduced with increasing post-smoothing.

To further study the effect of PSF on contrast recovery coefficients, we plot CRCmean and CRCmax against the ensemble noise in figure 10, so that we can compare the metrics for different reconstruction methods at a matched background noise level. For CRCmean, the PSF algorithm offers slightly improved (~7%) signal to noise performance over OSEM+LOR, and this benefit is present for all post-filtering parameters and sphere sizes. A similar improvement is also observed for CRCmax. Another interesting observation is made in figure 10. At the same CRCmean level, ensemble noise is reduced with the incorporation of PSF, and this effect is present for different post-filtering levels and ROI sizes.

Ensemble noise in hot spheres is shown in figure 11, and the patterns are similar to what we observed for background ensemble noise in figure 4. The noise goes up with iteration, and decreases with post-filtering and sphere size. Including PSF in the reconstruction has no difference on ensemble noise at matched iterations. Comparing figures 4 and 11, we observe that ensemble noise is lower in hot spheres than in background. Note that this is not to be confused with the standard deviation image results in figure 6, which shows larger sample standard deviation in hot spheres. Ensemble noise is defined as the coefficient of variation in equation (5), so the normalization term leads to smaller ensemble noise in hot spheres.

Results for SNR measures are presented in figure 12. Both SNRquant and SNRnpw increase with hot sphere size, indicating better quantitation and detection performance for larger objects. SNRquant goes down with increasing post-smoothing applied, and the amount of decrease is similar for each increase in post-filtering. SNRnpw has a ~30% increase from the unfiltered results when 4 mm post-filter is applied, but the performance is similar for post-smoothing parameters ranging from 4 mm to 10 mm. The difference trends of SNRquant and SNRnpw over post-filtering parameters indicate the distinction between quantitation and detection task performances. As for the effects of PSF modeling, the addition of PSF increases SNRquant by 20% for unfiltered data, and this improvement exists for all post-filtering and sphere sizes. For SNRnpw, including PSF offers slight improvement for large spheres (2–5% for the largest sphere, shown in the lower right image of figure 12). Detection performance for small objects is of more interest, and PSF modeling has shown modest improvement for smaller spheres. At iteration 5 for the 10 mm diameter sphere, including PSF increases SNRnpw by 16% for unfiltered data, and the increase is about 8% for the other 3 post-smoothing levels.

5. Discussion

The incorporation of PSF modeling into reconstruction affects image noise characteristics in different ways. Visual assessment from figures 2 and 3 suggests less noise for PSF-based reconstructions. At matched iterations, we observe PSF reconstruction has less noise in terms of image roughness and the standard deviation image (figures 4 and 6), but no significant difference is found for background variability or ensemble noise.

Image noise is quantified through noise variance and covariance. In section 3.1, we have derived how the background noise metrics relate to the ensemble noise variance and covariance. By comparing equations (15)–(17), we can explain why PSF modeling has different effects on the noise metrics. Since OSEM+LOR+PSF has a system model which relates each voxel to more measurement locations than the OSEM+LOR system model, the inverse problem is more ill-posed resulting in a slower convergence rate for OSEM+LOR+PSF. As a result, high-frequency components (including pixel variance) converge slower, so at matched iterations we would expect the pixel variance for a single voxel to be less for PSF versus non-PSF reconstruction. Our evaluation is across clinically acceptable range of iterations. Within this range and at matched iterations, we have observed smaller noise for PSF reconstruction (shown in figures 6 and 8), and this observation means that PSF-based reconstruction has smaller noise variance σ_b^2 at matched iterations. The addition of PSF also introduces larger noise correlation through the averaging process in the forward and backward projection model (shown in figure 8), implying that pixels would have positive correlation with their neighbors. As stated earlier, image roughness is affected by noise correlation. From equation (15), increased noise correlation due to PSF modeling, together with the effect of smaller σ_b^2, leads to smaller image roughness for PSF-based reconstruction at matched iterations (top row of figure 4). PSF modeling affects ensemble noise in a different manner. From equation (17), the reduction in noise variance is compromised by the increased noise correlation, so PSF modeling has no difference on ensemble noise at matched iterations. Equation (17) also shows that ensemble noise is more affected by the number of pixels in the ROI, and this is consistent with our observation that ensemble noise decreases with increasing ROI size (bottom right plot in figure 4).

Four different metrics have been used to quantify the noise properties in background. Among the metrics, image roughness and the standard deviation image are based on sample standard deviation of pixel values f_{ir}, so they are measures of pixel-to-pixel variation. Image roughness quantifies the variation from spatially correlated samples, while the standard deviation image measures the variation across independent realizations. The difference of these two metrics

can be understood from the plot of their ratio in figure 7 (the left plot). From equations (15) and (16), image roughness is affected by noise correlation while the normalized pixel standard deviation $EN_{onepixel}$ is not. The second term on the right-hand side of equation (15) measures the average pixel correlation in the ROI. For increased smoothing or smaller ROI size, the average correlation in the ROI increases, leading to smaller image roughness and hence a smaller ratio of the two metrics.

The other two noise metrics, background variability and ensemble noise, are based on the sample standard deviation of the ROI mean values, and thus are measures of region-to-region variation. Background variability quantifies the variation in the spatial domain, while ensemble noise captures the variation over different realizations. In figure 5 (bottom row), we observe a linear correlation between background variability and ensemble noise, and background variability appears to be slightly larger than ensemble noise. This phenomenon is also observed in figure 7 (the right plot), where the ratio of background variability and ensemble noise is greater than 1. Due to approximations in scatter correction and attenuation correction, the reconstructed image is not uniform in background. We observed from the mean image of 50 realizations that background activity is slightly lower in the center of the phantom, and such nonuniformity is similar for each realization. So spatial variation (measured by background variability) is larger than ensemble variation (measured by ensemble noise). Despite this difference between background variability and ensemble noise, a linear correlation of the two metrics exists for different combinations of reconstruction methods and parameters (figure 5). Due to the lack of multiple realizations of acquisitions, noise metrics defined on a single realization of data (e.g. background variability) are often used to assess performance of algorithms or system designs. The linear correlation between background variability and ensemble noise indicates that background variability is a reasonable surrogate for ensemble noise for the purpose of performance assessment when multiple realizations of data are not available.

Analysis in hot spheres shows improved contrast to noise performance with PSF modeling. Across a range of matched noise levels, OSEM+LOR+PSF offers roughly 7–12% improvement over OSEM+LOR in terms of contrast recovery coefficients (shown in figures 9 and 10), demonstrating the advantage of adopting more accurate system models in reconstruction. This improvement in signal recovery, combined with the reduction in noise variance, leads to modest improvement in SNRnpw (for small objects only) and SNRquant (shown in figure 12).

Several findings in our work are consistent with previous results in the literature. Panin *et al* (2006) showed that the incorporation of PSF into OSEM reconstruction leads to reduced pixel-to-pixel variation (similar to image roughness in our work). Several works have also shown that PSF-based reconstruction could improve contrast recovery (Bernardi *et al* 2007, Panin *et al* 2006, Jakoby *et al* 2009). Our work has systematically evaluated the noise and signal properties in PSF-based reconstruction across a range of reconstruction parameters. With access to 50 realizations of measured data, we evaluated the reconstruction algorithms with various noise and signal metrics. Some of the metrics we used, including ensemble noise, SNRquant and SNRnpw, could be calculated only when multiple realizations of data are available. Overall, we have found that PSF-based reconstruction has reduced noise variance and increased noise correlation at matched iterations, and the incorporation of PSF could also improve contrast recovery and SNR measures. The various metrics used in our work could further be related to major tasks of detection and estimation. For example, SNRnpw has been shown to correlate well with human observer detectability (Lartizien *et al* 2004, Kim *et al* 2003).

6. Conclusion

We have presented a systematic evaluation of noise and signal properties in different combinations of reconstruction methods and parameters for 3D PET image reconstruction. Our study is based on 50 sets of 3D PET data acquired on a clinical system. The data were reconstructed with two fully 3D reconstruction algorithms, OSEM+LOR and OSEM+LOR +PSF, in combination with four post-filtering options and 1–10 iterations, yielding 4000 image volumes for our analysis. With access to multiple realizations of data, we use four metrics to quantify the background noise properties, and five metrics to evaluate the signal and noise characteristics in features. Our evaluation is across clinically acceptable range of iterations. Among the four noise metrics, image roughness and standard deviations image are measures of the pixel-to-pixel variation, while background variability and ensemble noises quantify the region-to-region variation. At matched iterations, the incorporation of PSF results in images with less noise defined as image roughness and the standard deviation image, but it offers no significant difference for background variability or ensemble noise. PSF-based reconstructions have also shown improved signal to noise performance in terms of contrast recovery and SNR measures. We also study the relations of various noise metrics, and a linear correlation is observed between background variability and ensemble noise for all combinations of reconstruction methods and parameters. This correlation indicates that background variability is a reasonable surrogate for ensemble noise when multiple realizations of data are not available.

Acknowledgments

This work is supported by NIH grants HL086713, CA74135 and CA115870, a grant from GE Healthcare and the Society of Nuclear Medicine. The authors would like to thank C Stearns and S Ross for constructive discussions on image reconstruction.

References

Alessio, AM.; Kinahan, PE.; Harrison, RL.; Lewellen, TK. IEEE Nucl. Sci. Symp. Conf. Record; Puerto Rico. 2005. p. 1986-90.

Alessio AM, Kinahan PE, Lewellen TK. IEEE Trans Med Imaging 2006;25:828–37. [PubMed: 16827484]

Alessio AM, Stearns C, Tong S, Ross S, Kohlmyer S, Ganin A, Kinahan PE. IEEE Trans Med Imaging. 2010 to appear.

Barrett HH. J Opt Soc Am 1990;7:1266–78.

Barrett HH, Wilson DW, Tsui BMW. Phys Med Biol 1994;39:833–46. [PubMed: 15552088]

Bernardi ED, Mazzoli M, Zito F, Baselli G. IEEE Trans Nucl Sci 2007;54:1626–38.

Boellaard R, Krak NC, Hoekstra OS, Lammertsma AA. J Nucl Med 2004;45:1519–27. [PubMed: 15347719]

Comtat C, Kinahan PE, Defrise M, Townsend DW. IEEE Trans Nucl Sci 1998;45:1083–9.

Doot, RK.; Christian, PE.; Mankoff, DA.; Kinahan, PE. IEEE Nucl. Sci. Symp. Conf. Record; 2007. p. 2833-7.

Fessler JA. IEEE Trans Image Process 1996;5:493–506. [PubMed: 18285134]

Jakoby B, Bercier Y, Watson C, Bendriem B, Townsend D. IEEE Trans Nucl Sci 2009;56:633–9.

Jaskowiak CJ, Bianco JA, Perlman SB, Fine JP. J Nucl Med 2005;46:424–8. [PubMed: 15750154]

Kadrmas DJ. Phys Med Biol 2004;49:4731–44. [PubMed: 15566171]

Kadrmas DJ. IEEE Trans Med Imaging 2008;27:1071–83. [PubMed: 18672425]

Kadrmas DJ, Casey ME, Black NF, Hamill JJ, Panin VY, Conti M. IEEE Trans Med Imaging 2009;28:523–34. [PubMed: 19272998]

Kim JS, Kinahan PE, Lartizien C, Comtat C, Lewellen TK. SPIE Medical Imaging: Image Perception Observer Performance and Technology Assessment 2003:89–99.

Lartizien C, Kinahan PE, Comtat C. Acad Radiol 2004;11:637–48. [PubMed: 15172366]

Manjeshwar, RM.; Ross, SG.; Deller, TW.; Stearns, CW. IEEE Nucl. Sci. Symp. Conf. Record; 2006. p. 2804-7.

NEMA. NEMA Standards Publication NU 2-2001: Performance Measurements of Positron Emission Tomographs. Rosslyn, VA: National Electrical Manufacturers Association;

Panin V, Kehren F, Michel C, Casey M. IEEE Trans Med Imaging 2006;25:907–21. [PubMed: 16827491]

Qi J, Leahy R. IEEE Trans Med Imaging 2000;19:493–506. [PubMed: 11021692]

Qi J, Leahy RM, Cherry SR, Chatziioannou A, Farquhar TH. Phys Med Biol 1998;43:1001–13. [PubMed: 9572523]

Riddell C, Carson RE, Carrasquillo JA, Libutti SK, Danforth DN, Whatley M, Bacharach SL. J Nucl Med 2001;42:1316–23. [PubMed: 11535719]

Sharp, P.; Metz, C.; Wagner, R.; Myers, K.; Burgess, A. ICRU Report 54. Bethesda, MD: ICRU; 1996. Medical Imaging—The Assessment of Image Quality.

Soares EJ, Byrne CL, Glick SJ. IEEE Trans Med Imaging 2000;19:261–70. [PubMed: 10909922]

Soares EJ, Glick SJ, Hoppin JW. IEEE Trans Med Imaging 2005;24:112–21. [PubMed: 15638190]

Son HK, Yun M, Jeon TJ, Kim DO, Jung HJ, Lee JD, Yoo HS, Kim HJ. IEEE Trans Nucl Sci 2003;50:37–41.

Strul D, Slates RB, Dahlbom M, Cherry SR, Marsden PK. Phys Med Biol 2003;48:979–94. [PubMed: 12741496]

Wang W, Gindi G. Phys Med Biol 1997;42:2215–32. [PubMed: 9394408]

Wilson DW, Tsui BMW, Barrett HH. Phys Med Biol 1994;39:833–46. [PubMed: 15552088]

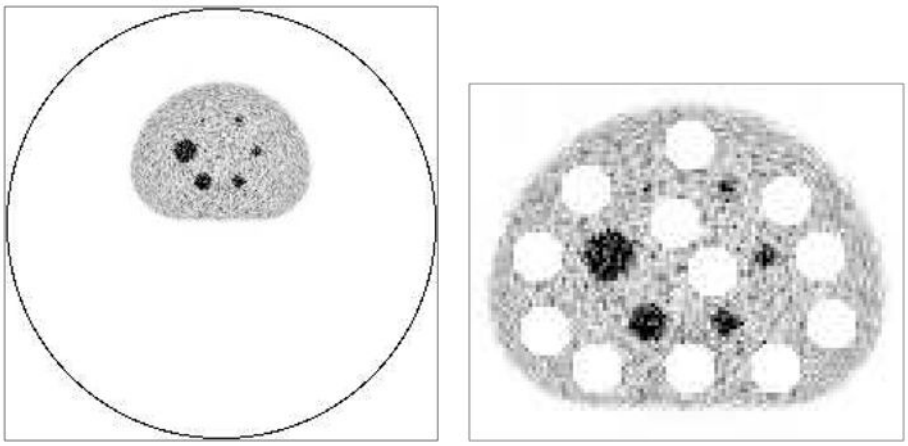

Figure 1.
(a) Example of one transaxial slice of reconstructed image (using OSEM+LOR reconstruction without post-filtering, iteration = 5), with the black circle denoting the scanner field of view; (b) NEMA background ROIs (denoted by white spheres) overlaid on a zoomed transaxial slice.

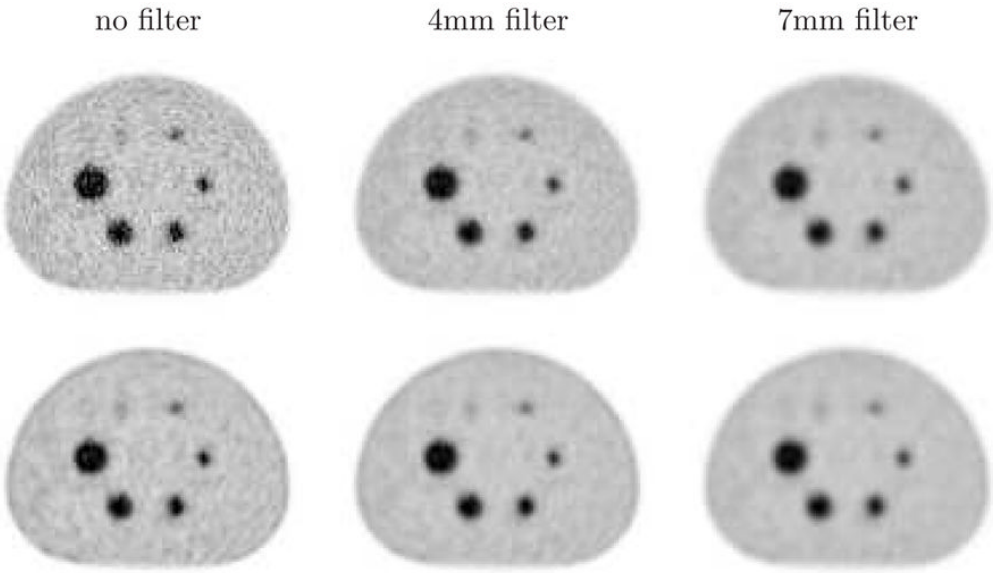

Figure 2.
Zoomed reconstructed images from one realization at iteration 2. Top: LOR; bottom: LOR +PSF. All images have the same color scale.

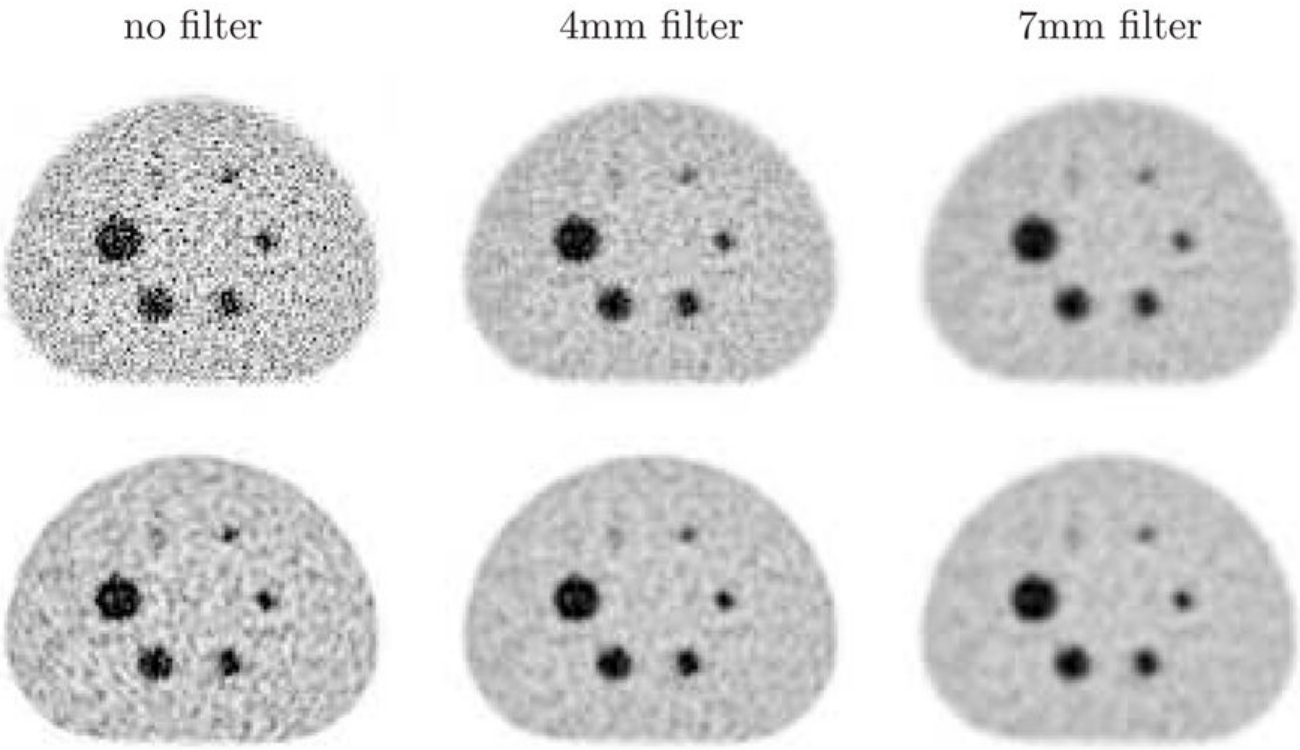

Figure 3.
Zoomed reconstructed images from one realization at iteration 8. Top: LOR; bottom: LOR +PSF. All images have the same color scale.

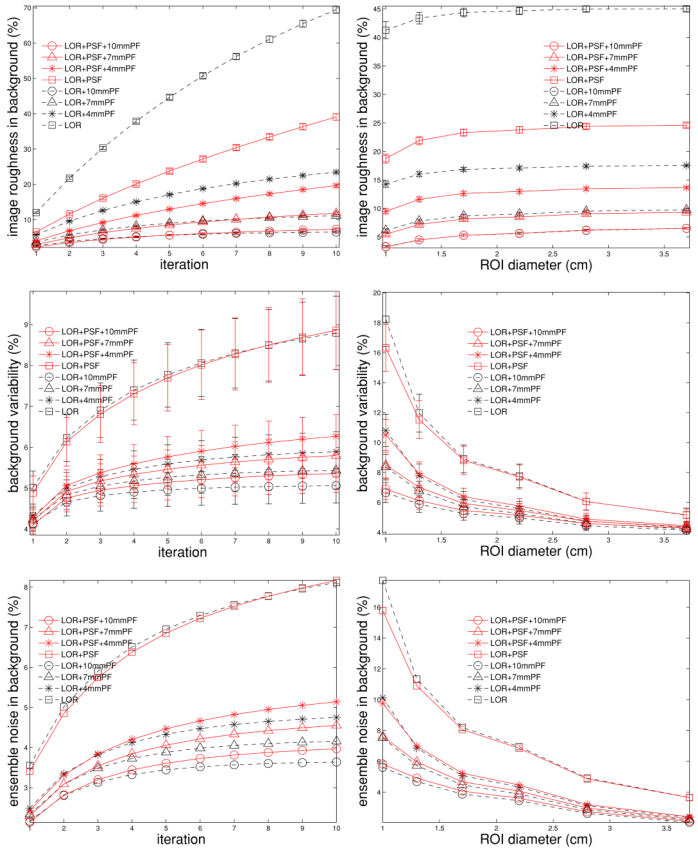

Figure 4.

Metrics for background noise. From top to bottom: image roughness, background variability, ensemble noise. Left column: noise metrics are plotted against iteration number with the ROI diameter fixed at 22 mm. Right column: noise metrics are plotted versus ROI size at fixed iteration 5. Error bars denote standard deviation across realizations.

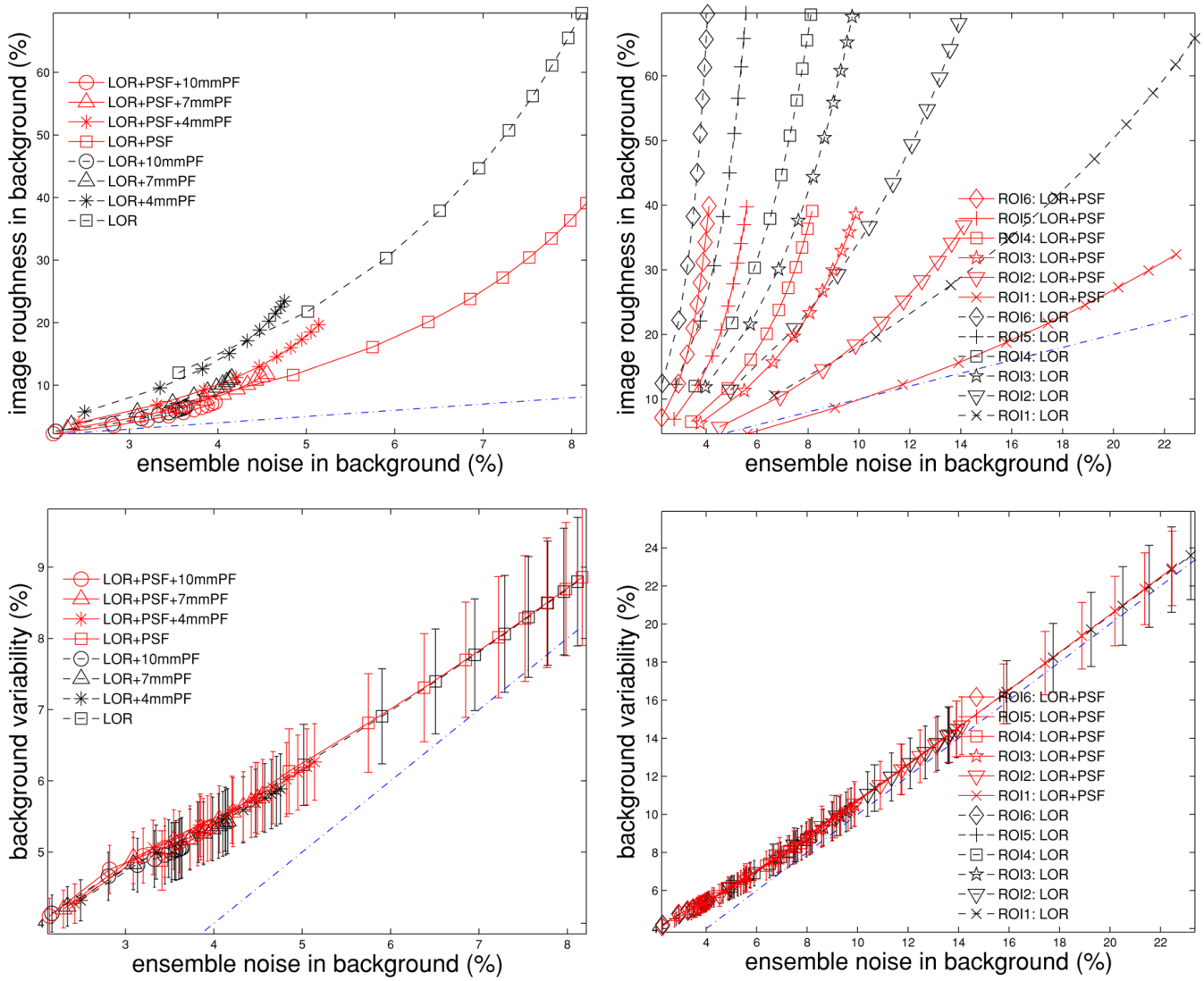

Figure 5.

Relations of noise metrics in background. From top to bottom: mean of image roughness (over realizations), and mean of background variability (over realization), plotted against the ensemble noise. Left column: relations of metrics are plotted with the ROI diameter fixed at 22 mm. Right column: relations of metrics are plotted for results without post-filtering. Error bars denote standard deviation across realizations, and the dash-dot line denotes the identity line.

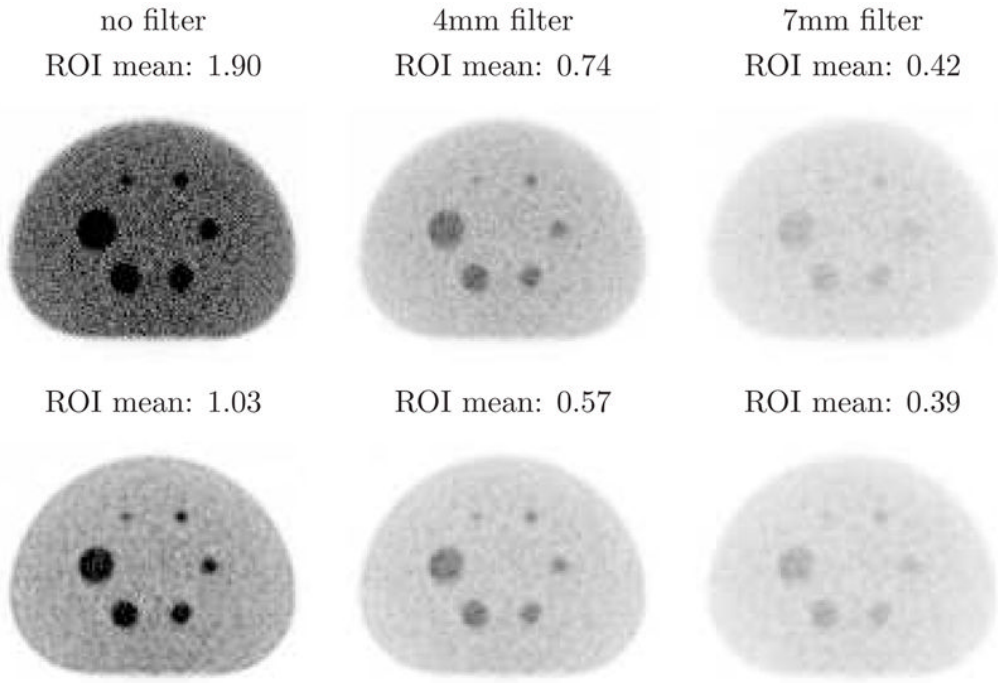

Figure 6.
The standard deviation image at iteration 5. Top: LOR; bottom: LOR+PSF. The ROI mean values of the background are shown above each corresponding image. All images have the same color scale.

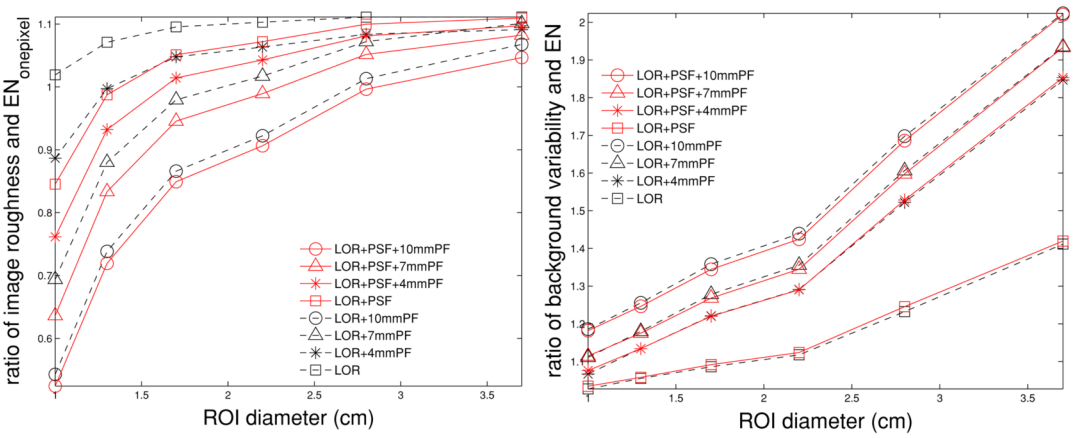

Figure 7.
Ratios of background noise metrics plotted versus ROI size at iteration 5. Left: ratio of image roughness and $EN_{onepixel}$. Right: ratio of background variability and ensemble noise.

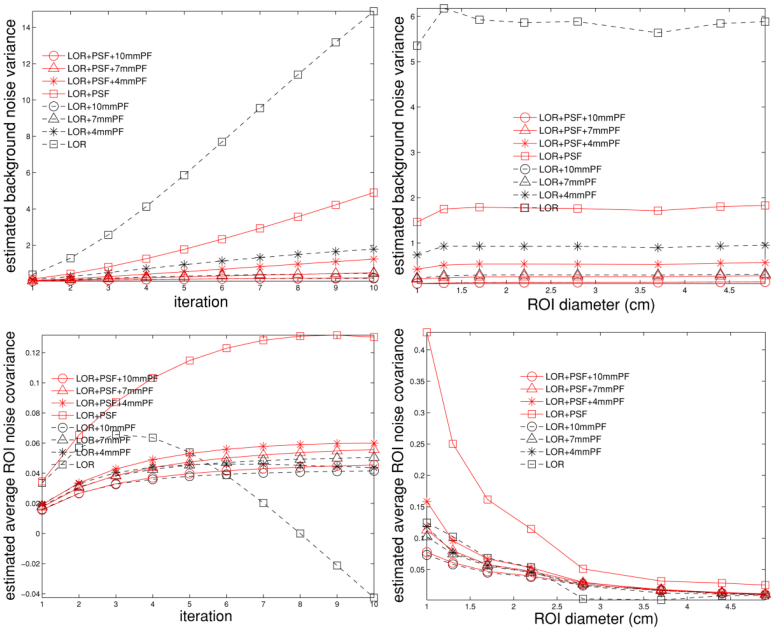

Figure 8.

Estimated background noise variance σ_b^2 (top) and average ROI noise covariance $\bar{C}$ (bottom). Left column: metrics are plotted against iteration number with the ROI diameter fixed at 22 mm. Right column: metrics are plotted versus ROI size at fixed iteration 5.

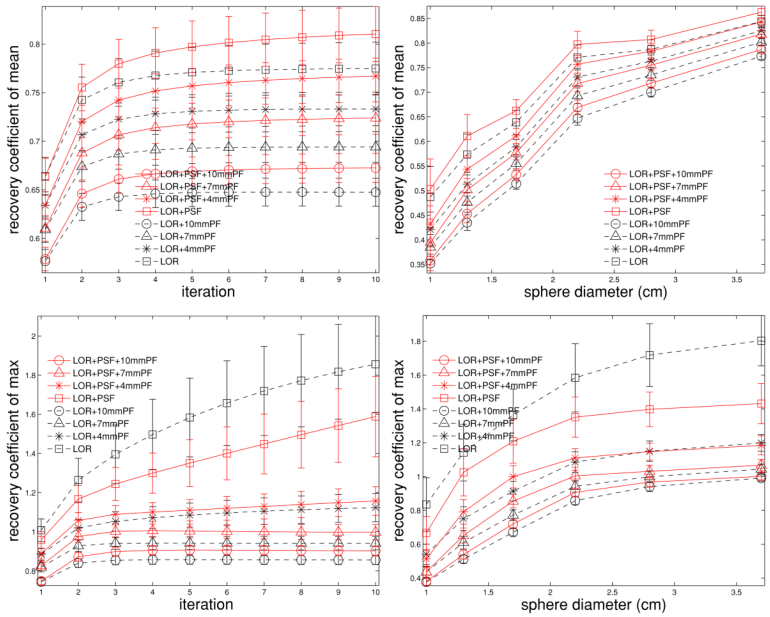

Figure 9.

Contrast recovery coefficient in hot spheres. From top to bottom: CRCmean, CRCmax. Left column: metrics are plotted against iteration number with the sphere diameter fixed at 22 mm. Right column: metrics are plotted versus sphere size at fixed iteration 5. Error bars denote standard deviation across realizations.

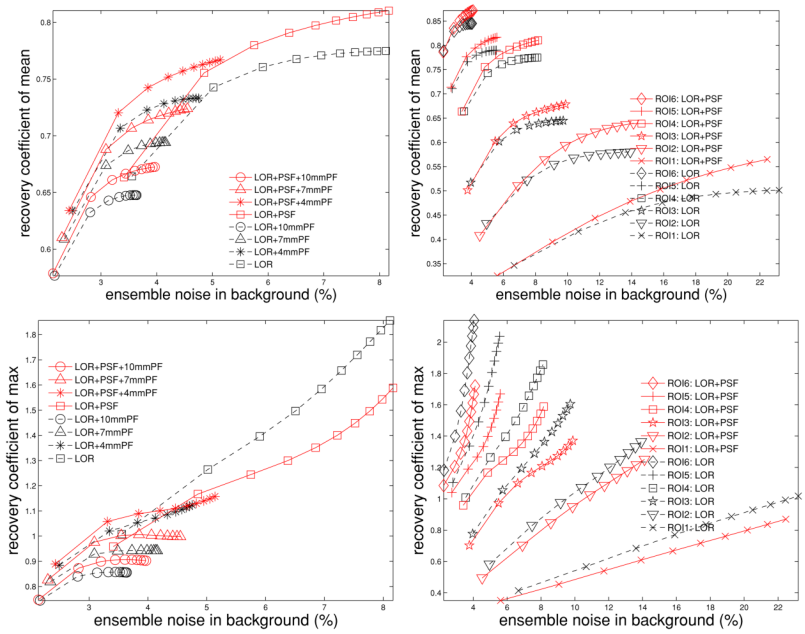

Figure 10.

Relations of recovery coefficient in hot spheres and background noise. From top to bottom: mean of CRCmean (over realizations), and mean of CRCmax (over realizations), plotted against ensemble noise in background. Left column: relations of metrics are plotted with the sphere diameter fixed at 22 mm. Right column: relations of metrics are plotted for results without post-filtering.

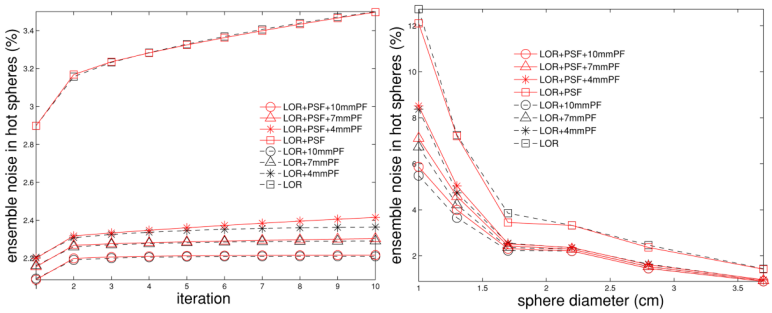

Figure 11.

Ensemble noise in hot spheres. Left: ensemble noise is plotted against iteration number with the sphere diameter fixed at 22 mm. Right: ensemble noise is plotted versus sphere size at fixed iteration 5.

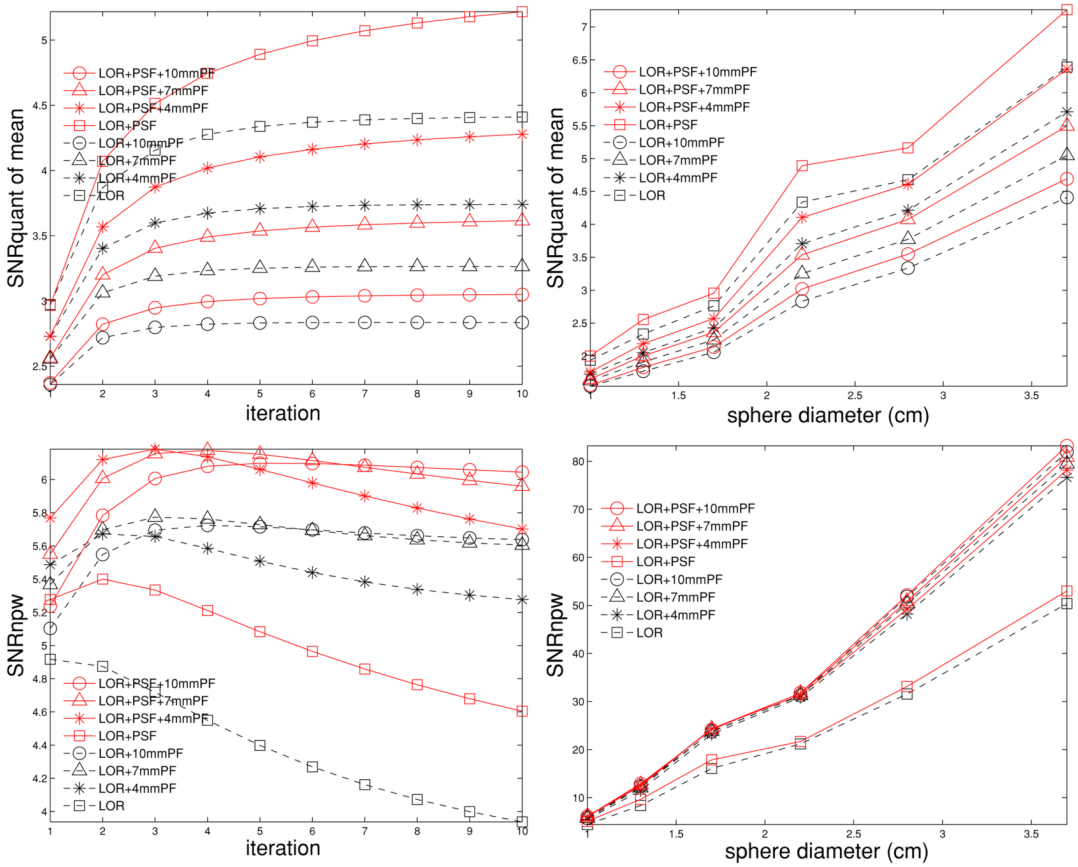

Figure 12.

SNR metrics of hot spheres. From top to bottom: SNRquant, SNRnpw. Left column: metrics are plotted against iteration number with the sphere diameter fixed (the sphere diameter is 22 mm for SNRquant, and 10 mm for SNRnpw). Right column: metrics are plotted versus sphere size at fixed iteration 5.